NUMERICAL INVESTIGATION OF NATURAL GAS FEASIBILITY IN A DIRECT INJECTION HEAVY-DUTY DIESEL ENGINE

by

Riad HADJAB[a] and Mahfoud KADJA[b]*

[a] Department of Drilling and Mechanic of Oil Yards, University of Kasdi Merbah, Ouargla, Algeria
[b] Laboratory of Applied Energetics and Pollution, Department of Mechanical Engineering,
University of Mentouri, Constantine, Algeria

In the present study, numerical simulations were performed on a direct injection heavy-duty Diesel engine. Methane, which is the predominant component in natural gas, was chosen as the fuel. The simulations involved five exhaust gas recirculation ratios (0%, 10%, 20%, 25%, and 30%) to examine their effect on engine performance, NO_x, and soot emissions. The numerical results were compared with existing experimental measurements of a typical Diesel engine without exhaust gas recirculation. A comparison of the numerical results of the four cases of exhaust gas recirculation ratios reveals that the 30% exhaust gas recirculation ratio achieves a significant reduction in NO_x emissions without increasing soot emissions. Consequently, the engine meets the authorized emission standards without excessive performance degradation.

Key words: *natural gas, Diesel engine, NO_x, soot, exhaust gas recirculation, FLUENT CFD*

Introduction

Natural gas is a promising alternative fuel for internal combustion engines because of its low emission potential, reasonable cost, and domestic availability. To match the performance and efficiency of conventional Diesel engines, the heavy-duty engine industry has adopted the technology of using natural gas in compression ignition engines. This technology is known as direct injection natural gas (DING) engines. In theory, it is possible to burn natural gas as a single fuel using a compression ignition engine. However, because of its high auto-ignition temperature, natural gas does not spontaneously ignite at the required time when injected into the combustion chamber of a typical Diesel engine. To overcome this challenge, a system for high pressure direct injection of natural gas and pilot diesel fuel was developed, where a small diesel pilot is injected first and ignites spontaneously from compression, followed shortly by natural gas injection, which is ignited by the diesel pilot's diffusion flame [1, 2]. In the long term, the most promising technology for heavy-duty engines is direct injection using natural gas as a single fuel, initiated using other separate ignition sources such as a spark plug or glow plug [3, 4]. This approach eliminates the need for a pilot diesel fuel and simplifies the combustion process, resulting in even lower emissions. The use of spark plug ignition assist has been suggested but was not considered suitable for such applications because of concerns over component durability [4]. Hot surface ignition assist is a recommended system for DING engines because it allows for the local increase of temperature in the combustion chamber without the

---

4102

Hadjab, R., *et al.*: Numerical Investigation of Natural Gas Feasibility in a …
THERMAL SCIENCE: Year 2024, Vol. 28, No. 5B, pp. 4101-4113

need for a complex two-fuel injector and two-fuel supply systems. From an environmental aspect, the advantage of using natural gas alone in a DING engine is that it generates less particulate matter than pilot diesel fuel. However, it is worth noting that both the DING engine and the pilot-injection natural gas engine generate NO_x in similar proportions. Hence, employing an aggressive exhaust gas recirculation (EGR) system for reducing NO_x in the DING engine is more feasible than in the pilot-injection natural gas engine, ensuring a satisfactory trade-off between particulate matter and NO_x emissions [5]. Several numerical studies on DING engines have been presented in the literature, such as those by Pan and Wallace [6-10], Papageorgakis [11], Korakianitis *et al.* [12], Ouellette [13], B. Yadollahi, M. Boroomand [14], and Kurniawan [15]. However, to the best of our knowledge, pollutant emissions, especially NO_x and soot, have rarely been studied numerically. The objective of this study is to investigate the combustion and emissions performance of a direct injection of natural gas into a Diesel engine. This study focuses on the effects of EGR on in-cylinder effective pressure, NO_x, and soot emissions [16-20]. Pure methane was used in this study because it represents the largest fraction (often 90% or more) of natural gas. In addition, the detailed chemical reactions involved in the simulations are simpler than those in higher-order hydrocarbon fuels.

Problem description

Tables 1 and 2 show the specifications and operating conditions for the engine, which have been previously employed in research related to combustion and pollutant emissions [21]. For this study, the amount of methane injected into the DING engine is set to 0.0666 gper cycle, whereas the typical amount of diesel fuel injected was set to 0.1622 g per cycle. This adjustment was made to approximately match the equivalent effective pressure (without EGR) of the diesel-fueled engine based on experimental results [21], as shown in fig. 1. The simulated simplified representation of fuel mass-flow profile is presented in fig. 2. The FLUENT CFD software is used in this study to simulate the non-premixed combustion process of a four-stroke Diesel engine [22], with methane as the fuel injected through the injector hole, as shown in fig. 3. The simulation involves introducing the main species of the EGR into the oxidant flow, with different EGR ratios (10%, 20%, 25%, and 30%) applied to examine their effect on engine performance, NO_x, and soot emissions.

Table 1. Engine specifications

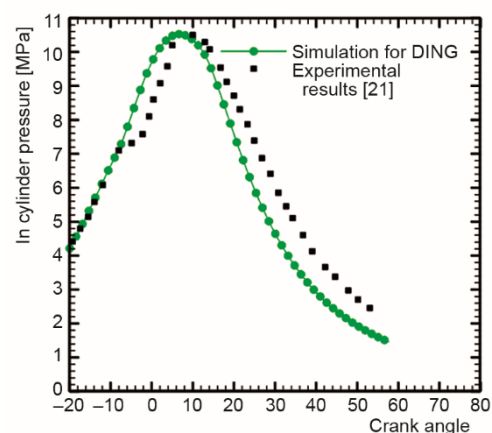| Engine	Caterpillar 3401
Cylinder bore × stroke [mm]	137.19 × 165.1
Compression ratio	15:1
Connected rod length [mm]	261.62
Combustion chamber geometry	Mexican hat
Engine speed (rpm)	1600
Intake valve closing (IVC)	−147 (aTDC)
Exhaust valve opening (EVO)	−136 (aTDC)

Figure 1. In-cylinder pressure for DING and a typical Diesel engine

Table 2. Fuel injection

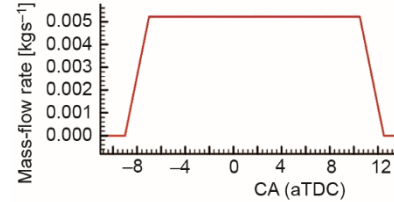| Number of nozzle holes	6
Nozzle hole diameter [mm]	0.259
Fuel injected [g per cycle]	0.1622
Start of injection (CA bTDC)	9°
Maximum injection pressure [MPa]	90
Injection duration (CA)	21.5

Figure 2. Simplified representation of fuel mass-flow profile

Computational domain and initial conditions

Figure 4 illustrates the geometry and calculation field of the simplified engine model. The problem considers a 60° periodic slice of the piston-cylinder combination, which corresponds to one fuel nozzle hole. The simulation begins at the IVC position and ends at the EVO position, with no valves, and only the compression and power stroke are simulated. To account for cyclic symmetry, a periodic boundary condition is applied to the front and back faces of the sector mesh, while a moving wall boundary condition is applied to the piston bowl. For internal combustion simulations, the piston in the TDC

Figure 3. Mesh of the injector hole

Figure 4. Mesh at the top dead center

position is recommended for meshing because it corresponds to the minimum volume position in the engine cycle. Establishing the mesh at this position ensures that the movement of the mesh is successful throughout the engine cycle. The mesh is then moved to the IVC position, which is the starting point of the simulation. The hexahedral mesh at the TDC was generated using ICEM software. The mesh contains 48478 cells with a minimum quality of 0.5. During the simulation, all meshes were generated using the FLUENT CFD software *via* a dynamic layering approach [22]. The mesh is deformed on the basis of the movement of the piston.
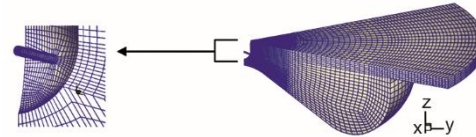
The initialization is performed at the IVC position, which corresponds to 147 bTDC.
- The initial pressure and temperature were estimated to be 190000 Pa and 300 K, respectively.
- The swirl ratio is set to 1.5 to initialize the swirl flow field in the combustion chamber using a UDF program provided by FLUENT CFD.
- The mass value of the fuel per cycle through the injector hole, the duration of injection, and the form of the injection rate are assigned in a UDF program provided by FLUENT CFD.
- The initial air mass and mass of the injected fuel change with the EGR as follows:

$$\text{Initial\_mass\_of\_air\_with\_EGR} = \text{initial\_mass\_of\_air\_without\_EGR} \times (1\text{-}R_{EGR}) \qquad (1)$$

$$\text{Fuel\_injected} = (\text{initial\_mass\_of\_air\_with\_EGR})/(\text{air/fuel})_{\text{actual}} \qquad (2)$$

- The mass fractions of each species of the oxidizer stream (air + EGR) when EGR is applied are calculated as follows:

$$Y_{(EGR+air)\_intake} = Y_{EGR\_exhaust} R_{EGR} + Y_{air\_intake}(1 - R_{EGR}) \qquad (3)$$

where $Y_{EGR+air\_intake}$ is the mass fraction of each species in the oxidizer stream, $Y_{EGR\_exhaust}$ − the mass fraction of each species in the EGR before its introduction in the oxidizer stream. These

4104

Hadjab, R., *et al.*: Numerical Investigation of Natural Gas Feasibility in a …
THERMAL SCIENCE: Year 2024, Vol. 28, No. 5B, pp. 4101-4113

mass fractions are calculated from global equations given in the appendix of [23] with excess-air ratio $\varphi_0 = 5$, Y_{air_intake} is the mass fraction of each species in air. The mass values of the fuel injected through the injector hole and the mass fraction of each species in the oxidizer stream for each EGR ratio are given in tab. 3.

Table 3. Mass of fuel through the injector hole according to the EGR

R_{EGR} [%]	Fuel injected [kg]	$Y_{O_2\_intake}$	$Y_{CO_2\_intake}$	$Y_{H_2O\_intake}$	$Y_{N_2\_intake}$
0	11.10×10^{-6}	0.23300	0	0	0.76700
10	09.99×10^{-6}	0.22726	0.00374	0.00306	0.76595
20	8.800×10^{-6}	0.2201	0.00839	0.00687	0.76464
25	8.326×10^{-6}	0.21581	0.01118	0.00915	0.76386
30	7.770×10^{-6}	0.21126	0.01414	0.01157	0.76303

Combustion modeling

Non-premixed model and computational sub-models

In this study, turbulent non-premixed combustion is used as a species model with a non-adiabatic energy option. Under the assumption of equal diffusivities, it involves the solution of transport equations for one or two conserved scalars, instead of solving the species equation for each species [24]. This conserved scalar is known as the mixture fraction. The standard k-ε model with standard wall functions is used as the viscous model, and the PISO algorithm is enabled for pressure-velocity coupling. All chemistry calculations are performed using the steady laminar flamelet sub-model, which simulates chemical non-equilibrium in non-premixed combustion [25, 26]. Based on detailed chemical mechanisms, the steady laminar sub-model is used in FLUENT CFD to predict the instantaneous relationship between the mixture fraction and thermochemical scalars such as species mass fractions, density, and temperature. These mechanisms are imported into FLUENT CFD using a Chemkin file consisting of 22 species and 104 elementary reactions.

Thermal NO_x and soot modeling

The thermal formation of NO_x is determined by a set of highly temperature-dependent chemical reactions, known as the extended Zeldovich mechanism [27, 28]. To predict soot emissions in FLUENT CFD, the Moss-Brookes model is selected because it was primarily developed and validated for methane flames. The Moss-Brookes model describes the evolution of soot through transport equations based on the soot mass fraction and the normalized nuclei concentration. The soot precursor is assumed to be acetylene C_2H_2, which plays a significant role in nucleation and surface growth [29]. The hydroxyl radical OH is assumed to be the dominant oxidizing agent in methane/air diffusion flames [30, 31].

Results and discussion

Velocity profiles

The velocity magnitude contours (case of EGR 0%) at various CA are presented in fig. 5. At the start of injection 9° bTDC, the swirl flow experiences minimal disturbance near the injector hole. Beyond this region, the velocity magnitude remains around 5-10 m/s. As injection proceeds, the fuel jet momentum progressively induces the flow field. At the TDC, the

Hadjab, R., *et al.*: Numerical Investigation of Natural Gas Feasibility in a …
THERMAL SCIENCE: Year 2024, Vol. 28, No. 5B, pp. 4101-4113

4105

fuel exits the injector hole at a velocity of 700 m/s, while the flame tip spreads across the bowl surface and reaches the bottom with a velocity of 56 m/s, generating a strong vertical flow that facilitates the rapid mixing of fuel and air. The swirl motion is largely dissipated at this CA position. It is clear from these results that despite having a higher exit velocity, the methane jet slows down quickly upon penetrating the combustion chamber because of its low density, gaseous state, and faster mixing with air, unlike diesel fuels [32]. A significant amount of methane diffuses from the core to the peripheries of the jet and reacts with O_2 *via* convective transport. This leads to higher temperatures at the jet periphery of methane. During the late stage of combustion (*e.g.*, 20° aTDC), the jet-induced motion is dissipated, and two vortices are formed, one close to the injector hole and the other above the bowl rim in the squish area. At CA corresponding to the downward movement of the piston (*e.g.*, 45° aTDC), the expansion flow dominates, the streamlines are directed downward in the bowl, and the maximum velocity magnitude values are located in the squish and the bowl pit areas.
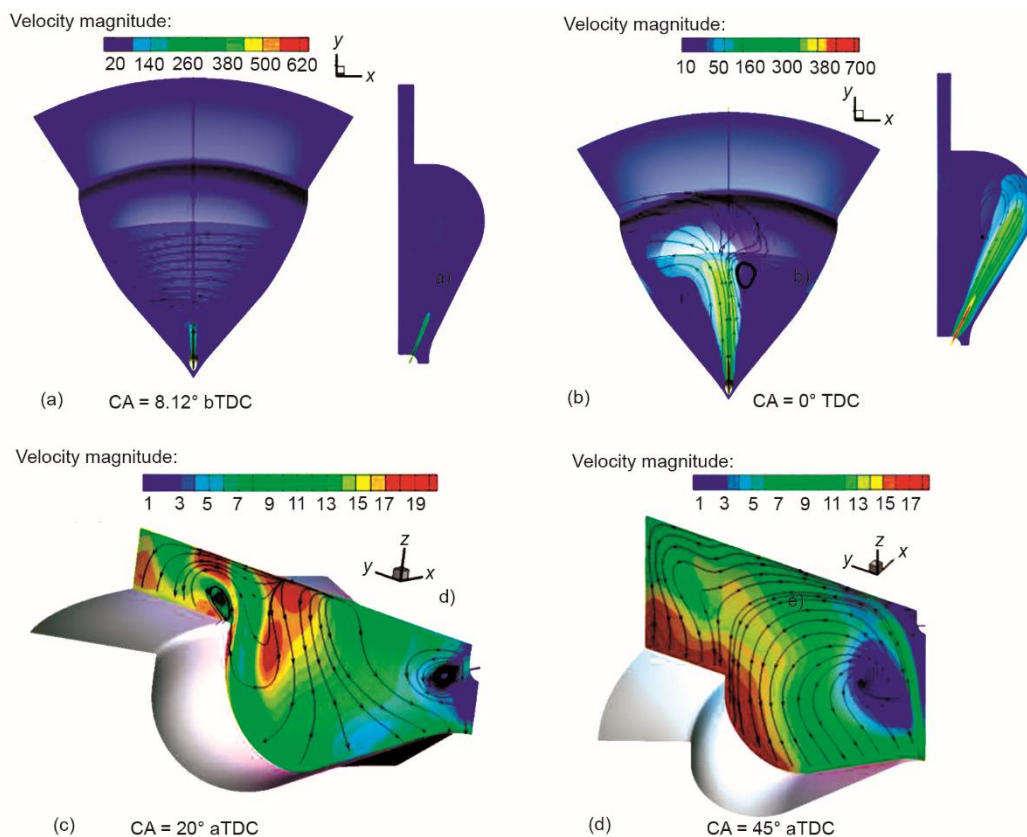

Figure 5. Contours of velocity magnitude at different crankshaft angles

Temperature profiles

Figures 6 and 7 illustrate, respectively, the in-cylinder temperature and the O_2 mass fraction contours (case of EGR 0%) at various crankshaft angles. In fig. 6, the temperature profiles

4106

Hadjab, R., *et al.*: Numerical Investigation of Natural Gas Feasibility in a …
THERMAL SCIENCE: Year 2024, Vol. 28, No. 5B, pp. 4101-4113

provide a realistic depiction of the combustion process occurring inside the combustion chamber, where the flame emanates from the injector hole. After the start of injection 9° bTDC, the flame surface initially attaches to the bottom of the bowl and then proceeds toward its edge, resulting in an upward direction of the flame. This induces a counterclockwise vortex flow, causing the flame surface to deform and diffuse into a larger area. As a result, a higher combustion temperature is distributed into the upper squish area and the piston bowl pit. Furthermore, due to the swirl effects, the symmetry of the flame around the injection axis is not maintained, which is noticeable at the TDC. The combustion process is shown to be heterogeneous because the temperature is higher and reaches approximately 2500 K in certain regions while remaining significantly lower in others. The temperature variation between these regions decreases as the piston moves down with values ranging from 1000 K to 1700 K. At the TDC position, the combustion process is in progress, resulting in a further rise in the maximum local temperatures, except in the low temperature zone, where the fuel-air ratio is high due to jet penetration. Around 13° aTDC, as depicted in fig. 2, the injection process concludes, leading to the cessation of the combustion process. This causes the local temperatures to peak (around 2500 K) in most parts of the flame. The maximum local temperatures stabilize and no longer increase. However, the residual heat produced by the combustion of the remaining injected fuel inside the combustion chamber continues to elevate the overall temperature until approximately 16° aTDC, as indicated by the red line in fig. 12 (0% EGR case). Figure 7 illustrates that the distribution of O_2 is inversely consistent with the temperature distribution. More specifically, after the end of the fuel injection at approximately 13° aTDC, regions with higher local temperature values have lower O_2 values and regions with lower local temperature values have higher O_2 values.
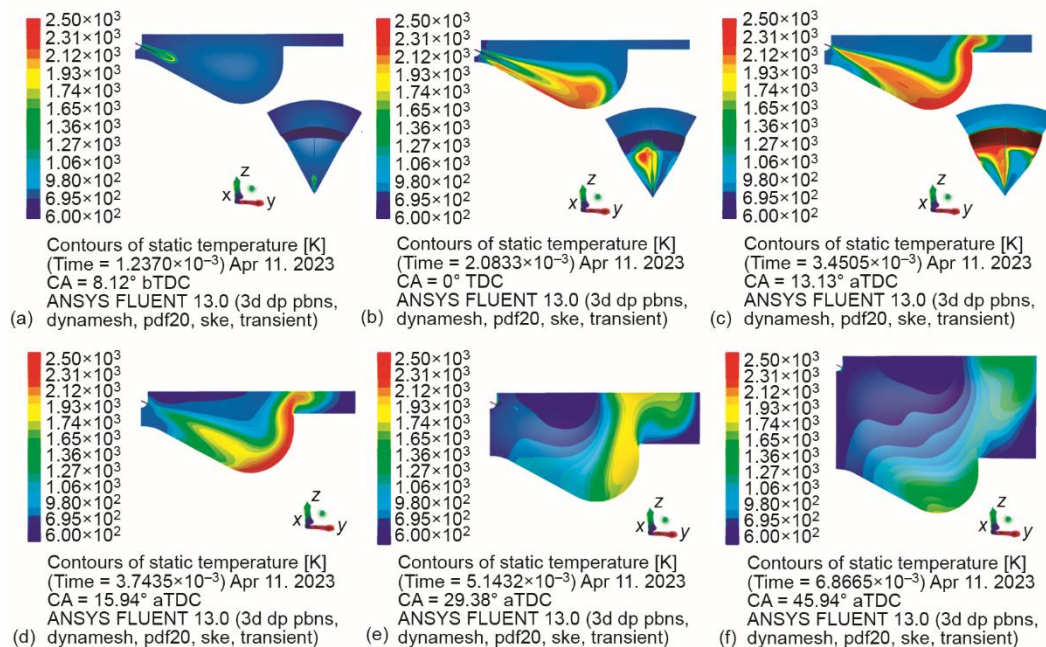

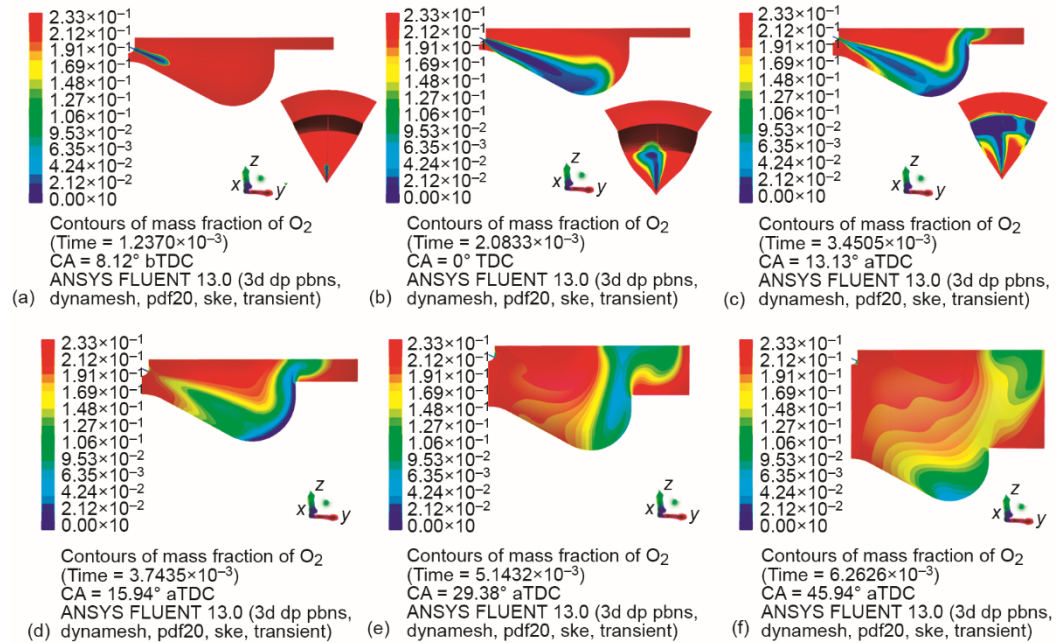**Figure 6. Temperature contours at different crankshaft angles**

Hadjab, R., *et al.*: Numerical Investigation of Natural Gas Feasibility in a ...
THERMAL SCIENCE: Year 2024, Vol. 28, No. 5B, pp. 4101-4113

4107

Figure 7. Contours of O$_2$ mass fractions at different crankshaft angles

The NO$_x$ emissions

Figure 8 depicts NO$_x$ contours (case of EGR 0%) that demonstrate the relationship between NO$_x$ emissions, temperatures, and O$_2$ in the cylinder, which is explained by the thermal mechanism of NO$_x$ formation. In the late phase of combustion, regions exposed to high temperatures and abundant in O$_2$ exhibit higher NO$_x$ levels. According to fig. 13, NO$_x$ becomes visible at approximately 8° aTDC position, which corresponds to the maximum in-cylinder mean pressure, as shown by the red line in fig. 11. At this stage, a higher temperature zone is located in the piston bowl pit, which is characterized by lower oxygen content, leading to the production of only a small amount of NO$_x$. At approximately 28° aTDC, NO$_x$ reaches its peak concentration, as shown by the red line in fig. 13. These NO$_x$ concentrations are located in two adjacent regions, one at the bottom of the bowl and the other around the squish area. Subsequently, in the expansion stage, the maximum local concentration of NO$_x$ decreases as the volume increases, while the overall amount of NO$_x$ in the cylinder remains constant, as shown in fig. 13.

Soot emissions

Figure 9 depicts the spatial evolution of the soot mass fractions (case of EGR 0%). The region with higher soot mass fractions is located near the bowl wall and is tilted from the middle plane owing to swirling motion. This observation is further supported by an examination of the velocity and temperature distributions shown in figs. 5 and 6, respectively. These soot contours exhibit a temporal trend similar to that of the soot curve (case of EGR 0%), as shown by the red line in fig. 14(a). Indeed, within the 3°-7° aTDC range, a localized area of soot begins to migrate within the bowl pit as the flame gradually expands toward the bowl rim. This migration is accompanied by a rapid increase in the overall soot mass, which peaks at approximately 7° aTDC. The increase in the soot mass fraction can be attributed to the increase in the C$_2$H$_2$ mass fraction, as shown in fig. 10. In the 7°-10° aTDC range, a rapid reduction of the soot

4108

Hadjab, R., *et al.*: Numerical Investigation of Natural Gas Feasibility in a …
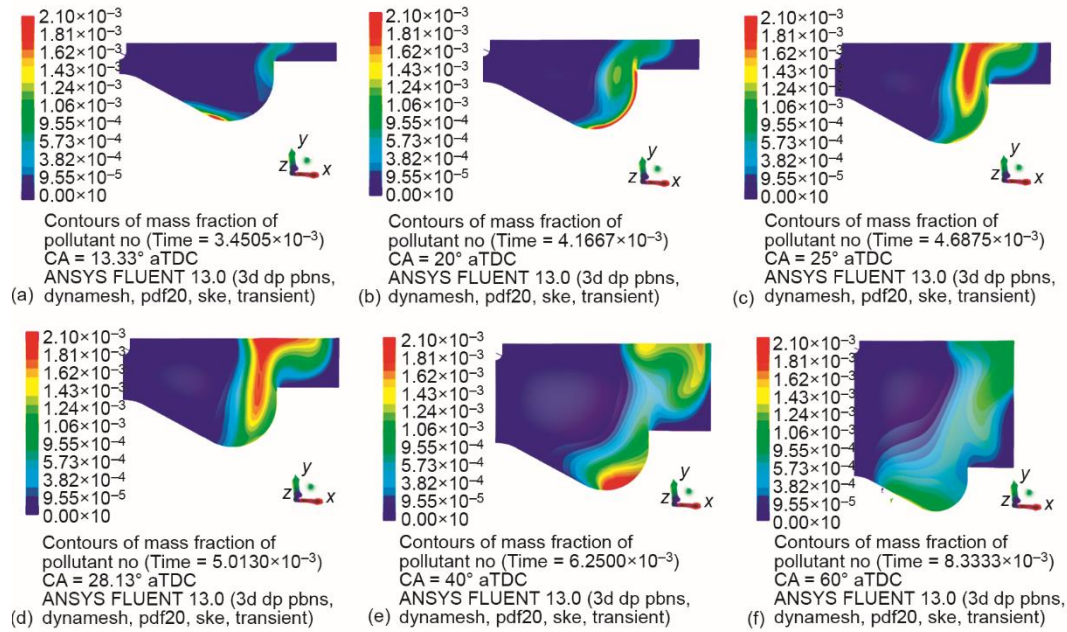THERMAL SCIENCE: Year 2024, Vol. 28, No. 5B, pp. 4101-4113

Figure 8. Contours of NO$_x$ mass fractions at different crankshaft angles

is observed on the bowl rim and then disappears as the CA position exceeds 10° aTDC. Consequently, there is an overall decrease in the soot mass within the cylinder during this period. This decrease can be attributed to C_2H_2 mass fraction, which starts to decline from the same position of 7° aTDC, as depicted in fig. 10. In the 10°-15° aTDC range, soot gradually expands within the bowl pit until approximately 15° aTDC, resulting in an increase in the overall soot mass once again, as shown in fig. 14(a). This increase in soot can be attributed to the decrease in fuel velocity penetration starting from the 10° aTDC position, as shown in fig. 2. The reduction in fuel velocity penetration may limit the rate of fuel-air mixing, thereby promoting the accumulation of soot.

On the other hand, soot is not observed in the core of the jet where the temperatures are lower. This can be attributed to the fact that high soot levels primarily exist in areas characterized by high temperatures and low oxygen levels, as shown in figs. 6 and 7. For instance, a relatively high soot mass fraction of 0.003 is localized within the temperature range of 2350-2450 K. From 15° aTDC position, soot experiences oxidation process simultaneously with the decline of the oxidant OH radicals and rapidly dissipates at approximately 20° aTDC, as shown in figs. 9 and 10. From 40° aTDC and during the expansion stage, only areas with low mass fractions of soot remain in the squish and the upper part of the combustion chamber. Furthermore, the level of soot formation is significantly lower than that of NO$_x$, as illustrated in figs. 8 and 9. This difference is particularly prominent during the expansion stage, where NO$_x$ emissions exceed soot emissions by more than 1000 times. This highlights the potential of natural gas as an effective means of reducing soot emissions, which can be largely attributed to the lower carbon content of natural gas compared with diesel fuels.
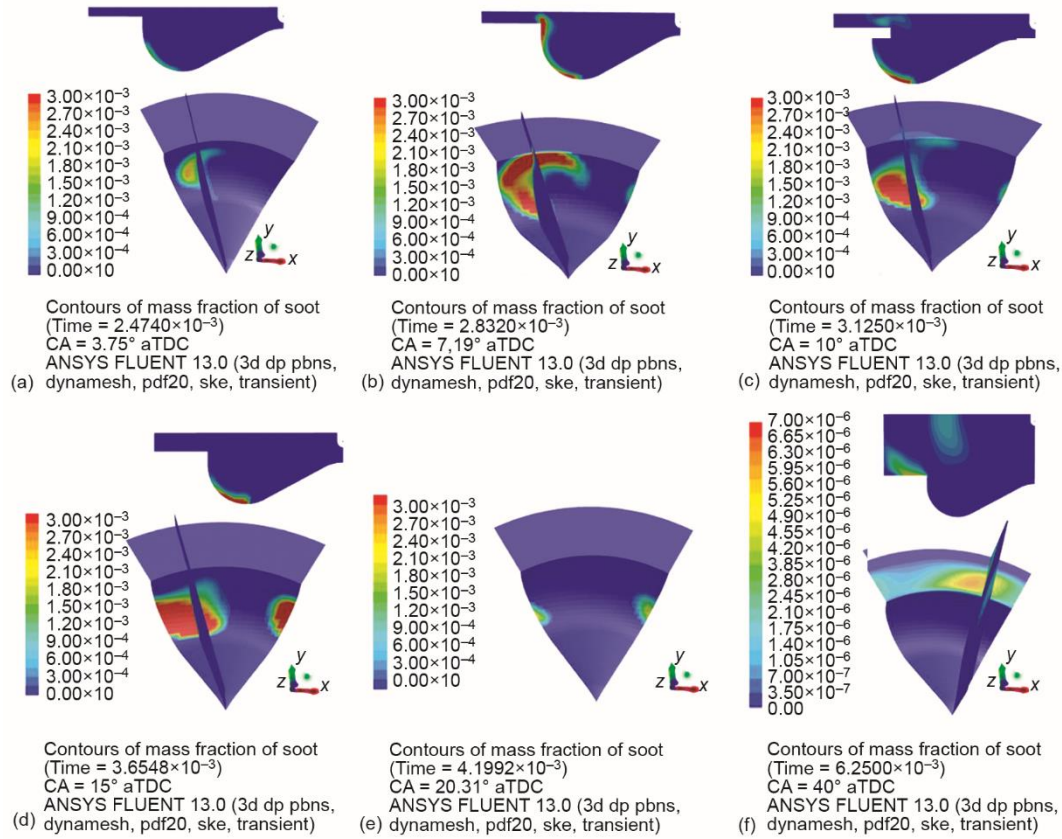
Hadjab, R., *et al.*: Numerical Investigation of Natural Gas Feasibility in a …
THERMAL SCIENCE: Year 2024, Vol. 28, No. 5B, pp. 4101-4113

4109

Figure 9. Contours of the soot mass fractions at different crankshaft angles

The EGR effect

In figs. 11 and 12, the in-cylinder mean pressure and mean temperature histories are displayed for the five EGR ratios (0%, 10%, 20%, 25%, and 30%). As shown in fig. 11, the peak of the mean pressure experiences a reduction of 0.87 MPa when the EGR ratio is increased from 0% to 30%, resulting in an 8% drop. Correspondingly, the peak of the mean temperature is lowered by 150 °C, leading to a 12% decrease. The reason is that when the EGR ratio is higher, the inert components lower the oxygen concentration in the cylinder. This slows down the combustion process and reduces both the peak of pressures and temperatures. Consequently, this leads to lower NO_x emissions.
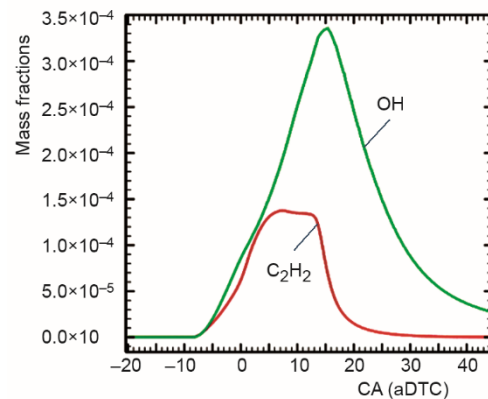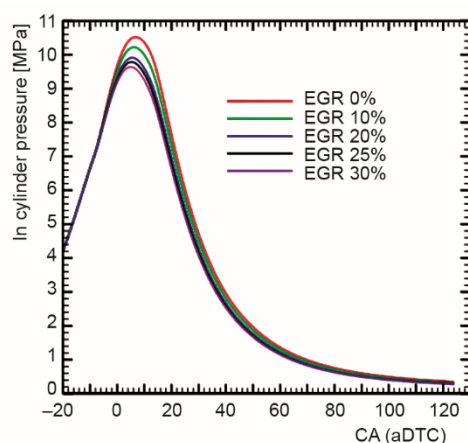

Figure 10. The OH and C_2H_2 mass fractions
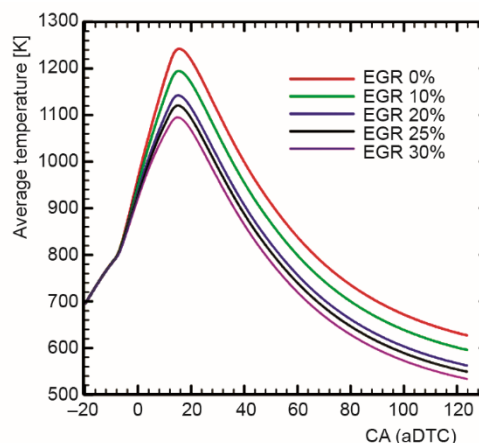
Figure 11. Mean pressure
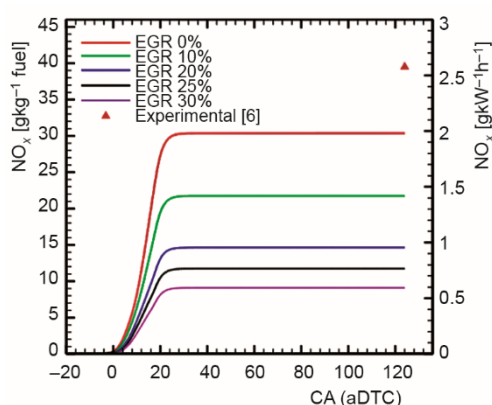

Figure 12. Mean temperature

Figure 13. The NO$_x$

Figure 13 illustrates the NO$_x$ emission history for the five EGR ratios. For the 0% EGR ratio, the formation of NO$_x$ starts at 4° bTDC and is frozen at its peak value at approximately 29° aTDC. As the EGR ratio increases, the initiation of NO$_x$ formation is progressively delayed and the rate of increase diminishes. Notably, engine-out NO$_x$ emissions exhibit a reduction of 70% when the EGR ratio is increased from 0% to 30%. This indicates the significant impact of EGR on mitigating NO$_x$ emissions from the engine. Moreover, the experimental engine-out NO$_x$ emissions from diesel fuel [21] are 30% higher than those from natural gas with 0% EGR ratio.

The amount of soot with respect to the CA for the five EGR ratios is presented in figs. 14(a) and 14(b) using both arithmetic and logarithmic scales. These plots provide clear evidence that as the EGR ratio increases, the amount of soot decreases. This finding contradicts the usual expectation that higher EGR ratios would lead to increased soot levels, especially when the amount of injected fuel is kept constant. This decrease in soot is primarily attributed to the decrease in the amount of fuel injected as the EGR ratio increases, despite the reduction in oxygen levels, as indicated in tab. 3. Moreover, the expanded distribution of the reduced injected fuel over the same injection duration enhances fuel and air mixing, resulting in reduced soot production. Analyzing the plot with an arithmetic scale for 0% EGR, it can be seen that the formation of soot begins at 2° aTDC, and the first peak value is quickly reached at approximately 7° aTDC. As the EGR ratio increases, the initiation of soot formation is progressively delayed, resulting in a gradual shift of the first peak values for each EGR ratio. However, the second peak values consistently occur at the same time for all EGR ratios, precisely at 15° aTDC. Furthermore, these second peak values become gradually lower than the first peak values for high EGR ratios. In addition, it is notable that the soot production rate for a 0% EGR

Hadjab, R., *et al.*: Numerical Investigation of Natural Gas Feasibility in a …
THERMAL SCIENCE: Year 2024, Vol. 28, No. 5B, pp. 4101-4113

4111

ratio is significantly higher than that for a 30% EGR ratio, resulting in a maximum soot mass approximately four times higher. From the plots with logarithmic scales in fig. 14(b), it can be observed that after soot production exceeds its maximum value, soot oxidation becomes the dominant process. The main stage of oxidation is characterized by a rapid reduction in soot levels and persists until approximately 22° aTDC. This initial stage is followed by a second stage, during which the soot oxidation rate uniformly slows for all cases of EGR, eventually converging to extremely low values. Comparing the engine-out of soot to its maximum value, it can be observed that approximately 99.64% of the soot mass is oxidized for 0% EGR ratio, whereas approximately 99.97% is oxidized for 30% EGR ratio. In addition, the experimental engine-out soot emissions from diesel fuel [21] are approximately 27 times higher than those from natural gas with 0% EGR ratio.
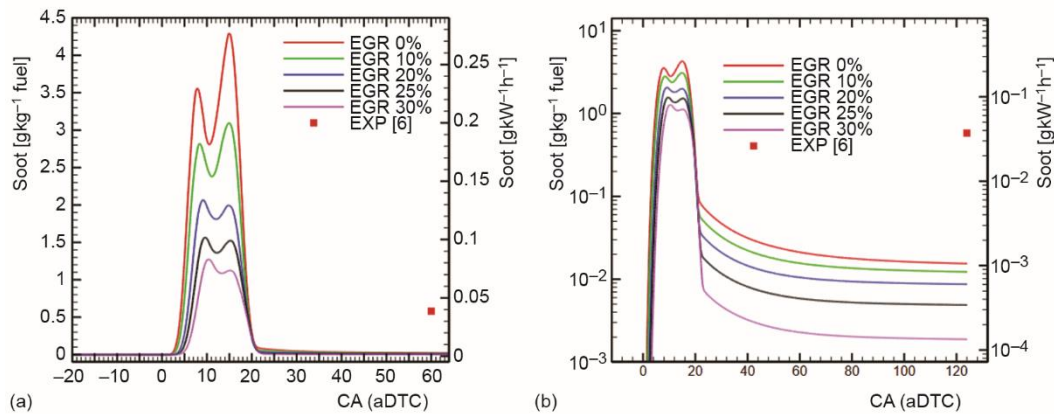

Figure 14. (a) Soot (arithmetic scales) and (b) soot (logarithmic scales)

Conclusions

To achieve a trade-off between NO_x and soot pollutants, various strategies inside the cylinder can be combined. In this study, two effective approaches were chosen for simulations: using natural gas (methane) as an alternate fuel and employing the EGR technique. The simulations used non-premixed turbulent combustion based on the flamelet approach. To predict pollutant emissions, the Zeldovich mechanism for thermal NO_x and the Moss-Brookes model for soot were employed. The study involved varying EGR ratios, specifically 0%, 10%, 20%, 25%, and 30%. The results of these simulations lead to a noteworthy conclusion: applying an EGR ratio of 30% allows for a significant reduction in NO_x emissions without an increase in soot emissions. Consequently, this approach enables agreement with authorized standards for heavy-duty engines without significantly compromising their performance. For further studies, it is recommended to extend the simulations to explore various engine parameters. These may include timing injection, mass rate of the injected fuel, rate injection shaping, optimization of combustion chamber shapes, injector diameter, and other relevant variables. By investigating these factors, researchers can gain a more comprehensive understanding of the effects of different engine configurations on emissions and engine performance. This will contribute to ongoing efforts to develop cleaner and more efficient Diesel engines that meet stringent emission regulations.

Nomenclature

CA   – crank angle
DING – direct injection of natural gas
EGR   – exhaust gas recirculation
EVO   – exhaust valve open
IVC   – intake valve close
R_{EGR} – exhaust gas recirculation ratio
Y_i – mass fraction of species i

Greek symbols

φ_0 – excess-air ratio

Subscript

i – species number

References

[1] Hodgins, B. K., *et al.,* Directly Injected Natural Gas Fuelling of Diesel Engines, SAE Paper No. 961671, 1996
[2] Gogolev, I. M., Wallace, J. S., Performance and Emissions of a Compression-Ignition Direct-Injected Natural Gas Engine with Shielded Glow Plug Ignition Assist, *Energy Conversion and Management, 164* (2018), May, pp. 70-82
[3] Vertin, K., Development of a Direct Injected Natural Gas Engine System for Heavy-Duty Vehicles, Final Report, Caterpillar, Inc, Peoria, Illinois, 2000
[4] Bartunek, B., Hilger, U., Direct Induction Natural Gas (DING): A Diesel Derived Combustion System for Low Emissions and High Fuel Economy, SAE International, 2000-01-2827, 2000
[5] Ladommatos, N., *et al.,* The Effects of Carbon Dioxide in Exhaust Gas Recirculation on Diesel Engine Emission, *Proceedings of the Institution of Mechanical Engineers, Part D: Journal of Automobile Engineering, 212* (1998), 1
[6] Pan, K., Wallace, J., Computational Studies of Fuel Injection Strategies on Natural Gas Combustion Characteristics in Direct-Injection Engines, *Fuel, 288* (2021), 119823
[7] Pan, K., Wallace, J. S., Numerical Studies of the Ignition Characteristics of a High pressure Gas Jet in Compression-Ignition Engines with Glow Plug Ignition Assist: Part 1 – Operating Condition Study, *Int. J. of Engine Res., 18* (2017) 10, pp. 1035-1054
[8] Pan, K., Wallace, J. S., Numerical Studies of the Ignition Characteristics of a High pressure Gas Jet in Compression Ignition Engines with Glow Plug Ignition Assist: Part 2 – Effects of Multi-Opening Glow Plug Shields, *Int. J. of Engine Res., 19* (2018) 9, pp. 977-1001
[9] Pan, K., Wallace, J. S., Soot and Combustion Models for Direct-Injection Natural Gas Engines, *Int. J, Engine Res. 23* (2020) 1, pp. 150-166
[10] Pan, K., Wallace, J. S., A Low Temperature Natural Gas Reaction Mechanism for Compression Ignition Engine Application, *Combust Flame, 202* (2019), Apr., pp 334-346
[11] Papageorgakis, G., *et al.,* Multi-Dimensional Modeling of Natural Gas Injection, Mixing and Glow Plug Ignition Using the Kiva-3 Code, American Society of Mechanical Engineers, New York, NY (United States), Tech. rep., 1996
[12] Korakianitis, T., *et al.,* Natural-Gas Fueled Spark-Ignition (SI) and Compression Ignition (CI) Engine Performance and Emissions, *Prog. Energy Combust. Sci., 37* (2011) 1, pp. 89-112
[13] Ouellette, P., *et al*., Numerical Simulations of Directly Injected Natural Gas and Pilot Diesel Fuel in a Two-Stroke Compression Ignition Engine, SAE Technical Paper 981400, 1998
[14] Yadollahi, B., Boroomand, M., A Numerical Investigation of Combustion and Mixture Formation in a Compressed Natural Gas DISI Engine with Centrally Mounted Single-Hole Injector, *J. Fluids Eng., 135* (2013), 9, 091101
[15] Kurniawan, W. H., Abdullah, S., Numerical Analysis of the Combustion Process in a Four-Stroke Compressed Natural Gas Engine with Direct Injection System, *J. Mech. Sci. Technol., 22* (2008), Mar., pp. 1937-1944
[16] Khatamnezhad, H., *et al.,* Incorporation of EGR and Split Injection for Reduction of NOx and Soot Emissions in DI Diesel Engines, *Thermal Science, 15* (2011), Suppl. 2, S409-S427
[17] Nemati, A., *et al.*, Decreasing the Emissions of a Partially Premixed Gasoline Fueled Compression Ignition Engine by Means of Injection Characteristics and EGR, *Thermal Science, 15* (2011), 4, pp. 939-952
[18] Mohamed, B., *et al.*, Numerical Analysis of Injection Parameters Influence on Diesel Engine Performances and Emissions Correlated by Maximum In-Cylinder Pressure, *Thermal Science, 27* (2023), 2B, pp. 1479-1493

Hadjab, R., *et al.*: Numerical Investigation of Natural Gas Feasibility in a …
THERMAL SCIENCE: Year 2024, Vol. 28, No. 5B, pp. 4101-4113

4113

[19] He, Z., *et al.*, A Numerical Study of the Effects of Injection Rate Shape on Combustion and Emission of Diesel Engines, *Thermal Science, 18* (2014), 1, 67-78

[20] Zhi-Qiang, Z., *et al.*, A Simulated Study on the Performance of Diesel Engine with Ethanol-Diesel Blend Fuel, *Thermal Science, 17* (2013), 1, pp. 205-216

[21] Binesh, A. R., *et al.,* Three-Dimensional Modeling of Mixture Formation and Combustion in a Direct Injection Heavy-Duty Diesel Engine, *Int. Journal of Aerospace and Mechanical Engineering, 2* (2008), 4, pp. 214-219

[22] ***, ANSYS Inc. FLUENT User Guide and FLUENT Theory Guide, version 13.0, 2010

[23] Hadjab, R., Kadja, M., Computational Fluid Dynamics Simulation of Heat Transfer Performance of Exhaust Gas Re-Circulation Coolers for Heavy-Duty Diesel Engines, *Thermal science, 22* (2018) 6B, pp. 2733-2745

[24] Sivathanu, Y. R., Faeth, G. M., Generalized State Relationships for Scalar Properties in Non-Premixed Hydrocarbon/Air Flames, *Combustion and Flame, 82* (1990), 2, pp. 211-230

[25] Bray, K. N., Peters, N., Laminar Flamelets in Turbulent Flames, in: (P. A. Libby and F. A. Williams, eds.), *Turbulent Reacting Flows,* Academic Press, New York, USA, 1994, pp. 63-114

[26] Peters, N., Laminar Diffusion Flamelet Models in Non Premixed Combustion, *Prog. Energy Combust. Sci. 10* (1984) 3, pp. 319-339

[27] Baulch, D. L., *et al., Evaluated Kinetic Data for High Temperature Reactions,* Butterworth, New York, USA, 1973

[28] Hanson, R. K., Salimian, S., Survey of Rate Constants in H/N/O Systems, in: (W. C. Gardiner, ed.), *Combustion Chemistry, 361,* New York, USA, 1984

[29] Brookes, S. J., Moss, J. B., Prediction of Soot and Thermal Radiation in Confined Turbulent Jet Diffusion Flames, *Combustion and Flame, 116* (1999), 4, pp. 486-503

[30] Fenimore, C. P., Jones, G. W., Oxidation of Soot by Hydroxyl Radicals, *J. Phys. Chem., 71* (1967) 3, pp. 593-597

[31] Babayev, R., *et al,* Computational Comparison of the Conventional Diesel and Hydrogen Direct-Injection Compression-Ignition Combustion Engines, *Fuel, 307* (2022), 121909